condensed
matter

MDPI

Article

Detection of Surface States in Quantum Materials $ZrTe_2$ and TmB_4 by Scanning Tunneling Microscopy

Maria Victoria Ale Crivillero [1], Jean C. Souza [1,2,†], Vicky Hasse [1], Marcus Schmidt [1], Natalya Shitsevalova [3], Slavomir Gabáni [4], Konrad Siemensmeyer [5], Karol Flachbart [4] and Steffen Wirth [1,*]

[1] Max Planck Institute for Chemical Physics of Solids, Nöthnitzer Straße 40, 01187 Dresden, Germany
[2] Instituto de Física "Gleb Wataghin", Unicamp, Campinas 13083-859, SP, Brazil
[3] Institute for Problems of Materials Science, NASU, Krzhyzhanovsky Str. 3, 03142 Kyiv, Ukraine
[4] Institute of Experimental Physics, SAS, Watsonova 47, 04001 Košice, Slovakia
[5] Helmholtz Zentrum Berlin, 14109 Berlin, Germany
* Correspondence: steffen.wirth@cpfs.mpg.de
† Current address: Weizmann Institute of Science, Rehovot 7610001, Israel.

Abstract: Scanning Tunneling Microscopy and Spectroscopy (STM/S), with its exceptional surface sensitivity and exquisite energy resolution, is well suited for the investigation of surface states down to atomic length scales. As such, it became an essential tool to probe the surface states of materials, including those with non-trivial topology. One challenge, however, can be the preparation of clean surfaces which allow the study of preferably unchanged surface properties with respect to the bulk amount. Here, we report on the STM/S of two materials, $ZrTe_2$ and TmB_4. The former cleaves easily and defects can be examined in detail. However, our STS data can only qualitatively be compared to the results of band structure calculations. In the case of TmB_4, the preparation of suitable surfaces is highly challenging, and atomically flat surfaces (likely of B-termination) were only encountered rarely. We found a large density of states (DOS) at the Fermi level E_F and a mostly featureless differential conductance near E_F. Further efforts are required to relate our results to the electronic structure predicted by ab initio calculations.

Keywords: Scanning Tunneling Microscopy; surface states; topology

check for updates

Citation: Ale Crivillero, M.V.; Souza, J.C.; Hasse, V.; Schmidt, M.; Shitsevalova, N.; Gabáni, S.; Siemensmeyer, K.; Elachbart, K.; Wirth, S. Detection of Surface States in Quantum Materials $ZrTe_2$ and TmB_4 by Scanning Tunneling Microscopy. *Condens. Matter* **2023**, *8*, 9. https://doi.org/10.3390/condmat8010009

Academic Editors: Ali Gencer, Annette Bussmann-Holder, J. Javier Campo Ruiz and Valerii Vinokur

Received: 23 December 2022
Revised: 11 January 2023
Accepted: 12 January 2023
Published: 16 January 2023

1. Introduction

The interpretation of the quantum Hall effect, in terms of topology, has been well established for several decades [1]. More recently, the quantum spin Hall effect was predicted [2,3] and realized soon after [4]. These discoveries were followed by huge developments in the field of non-trivial topology, including materials such as topological insulators, semimetals and superconductors [5–8]. In particular, enormous efforts were undertaken to predict non-trivial topology in materials, see [9] and references therein. In this respect, both spin-orbit coupling and crystalline symmetry, as well as their interplay, are of particular importance.

Likewise, there have also been tremendous efforts to experimentally investigate and/or verify non-trivial topology in these materials. One of the primary tools here is angle-resolved photoemission spectroscopy (ARPES) as it can provide information on the materials' electronic structure [10–14], in some cases even in a spin-resolved fashion [15–17]. As an example, ARPES can reveal the linear dispersion relation expected for electrons on a Dirac cone. One other method of choice is Scanning Tunneling Microscopy and Spectroscopy (STM/S) with its ability to get *local* insight into the single-particle spectrum [18]. It is extremely surface sensitive and can be conducted at ultra-low temperatures, in magnetic fields and with energy resolution in the meV-range or even below. As such, STM/S is well suited to investigate surfaces of topological quantum matter [19–21], specifically in cases where the involved energy scales are as small as in the correlated topological insulators SmB_6 [22].

As a result of the extreme surface sensitivity of STM, a clean and atomically flat surface is often required for the successful spectroscopic analysis of the material's electronic structure: if the investigated surface is rough on an atomic level, then the local environment of the surface atoms may differ from the one of the same atom in the bulk. Of course, this issue adds to the already incurred modified material properties at the surface of any solid (see e.g., the discussion in [23]) or possible surface reconstructions. As a consequence, special attention may have to be paid to the preparation of clean surfaces for STM investigations. Established methods here are in situ deposition of thin films or in situ cleaving of bulk samples. The latter can easily be conducted on van-der-Waals-bound layered materials (like Bi_2Te_3 [24]). However, for materials with a more three-dimensional (3D) crystallographic structure (like SmB_6 [25]) cleaving can be a challenge. It should be noted that surface preparation for ARPES measurements is not quite as involved as for STM but it may need to receive some attention nonetheless [26].

We here report on STM investigations on two materials: $ZrTe_2$ and TmB_4. The former is a member of the extensively studied group of transition-metal dichalcogenides [27] and is discussed as a topological Dirac semimetal [28–31]. Moreover, signatures of a weak Kondo effect have been reported [32]. On the other hand, the material TmB_4 crystalizes in a Shastry–Sutherland lattice which gives rise to frustrated magnetic behavior and, in particular, to fractional plateaus in its magnetization curves [33]. Interestingly, topology is mentioned as one possible reason for the fractional plateau phase [34,35], and the related compound PuB_4 is discussed to be a strong topological insulator [36]. For both materials, our spectroscopic results by STS reveal substantial discrepancies compared to the results of bulk band structure calculations. These discrepancies are likely (at least in part) related to the extreme surface sensitivity of STS and highlight the need for further experimental and theoretical efforts to gain a comprehensive understanding of such materials, specifically with respect to applications.

2. Samples and Experiments

In the first synthesis step, microcrystalline $ZrTe_2$ was obtained starting from a molar powder mixture of the elements zirconium (99.2% Alfa Aesar) and tellurium (99.999% Alfa Aesar) annealed at 600 °C in the presence of iodine (99.998% Alfa Aesar) in an evacuated fused silica ampoule for one week. In the second step, single crystals of $ZrTe_2$ were grown from this microcrystalline powder by chemical vapor transportation with iodine (4 mg/mL) as a transport additive. Here, a temperature gradient from 700 °C (source with starting material) to 800 °C (sink with deposited crystals) was applied. Single crystals grew in the shape of well-formed, several mm wide platelets along the crystallographic a–b directions with heights (along c) of order 0.2 mm. The characterization of the single crystals was conducted by electron probe microanalysis (EDXS) and X-ray powder diffraction; the latter confirmed the hexagonal structure (space group $P\bar{3}m1$ with lattice constants $a = 3.952$ Å and $c = 6.66$ Å), see Figure S1. For STM, $ZrTe_2$ was cleaved along the crystallographic c direction, i.e., by breaking the van-der-Waals bonds.

TmB_4 samples were cut from a single crystalline rod grown by an inductive, crucible-free-zone melting method described in detail in [37] (see also Supplementary Materials Section II and Figures S2 and S3). The lattice constants of the tetragonal lattice (space group $P4/mbm$, see Figure 1) are $a = 7.05$ Å and $c = 3.98$ Å. For STM measurements, samples were attempted to cleave along the ab plane.

STM investigations were conducted using an ultra-high vacuum (UHV) system [38]. If not stated otherwise, the presented STM/STS data were obtained at its base temperature of $T = 4.6$ K using electrochemically etched tungsten tips. STS was performed by utilizing a lock-in technique; to this end, a small ac modulation voltage V_{mod} of 1.0 mV with a frequency of 117 Hz was added to the bias voltage V_{b}. In some cases, the reported STM data were obtained in a dual-bias mode, i.e., two different bias voltages (typically of opposite sign) were applied for the forward and backward scan of the fast scan direction. Bias voltage V_b and set-point current I_{sp} are given in the respective caption of each topography.

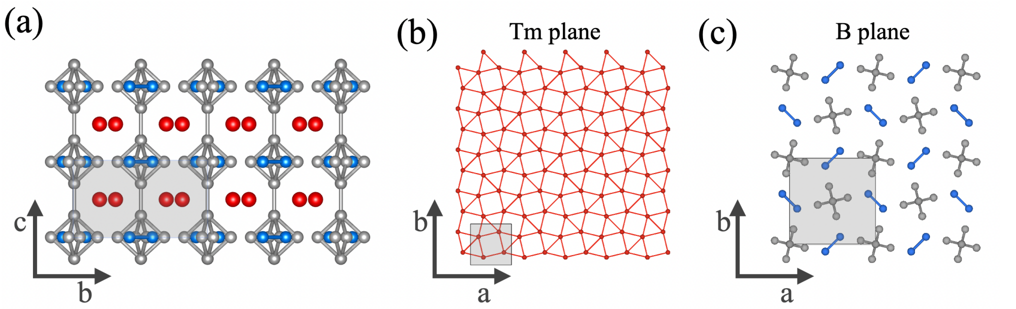

Figure 1. Crystalline structure of tetragonal TmB_4. (**a**) View along the *bc* plane; red: Tm, gray: B octahedra, blue: B dimers. (**b**) Tm plane visualizing the combination of square and triangular arrangements. (**c**) B atoms in the *ab* plane. All panels share the same color code, with one unit cell marked in gray.

To avoid possible degradation, the $ZrTe_2$ sample investigated here was stored and prepared for cleavage inside an Ar-filled glove box. All samples were cleaved in situ at a temperature of ∼20 K. After cleaving, the samples needed to be transferred from the cleaving stage into the STM head, during which time (few tens of seconds) the sample temperature is not controlled. Because of its layered structure, $ZrTe_2$ cleaves easily and is exposed to large atomically flat surface areas. We, therefore, investigated one cleaved surface at numerous different positions. In contrast, TmB_4 is very difficult to cleave and atomically flat areas could be found only rarely (see also Section 3.2.1 below). In order to, nonetheless, ensure the reproducibility of our results, cleaves of three TmB_4 samples were studied.

3. Results

3.1. $ZrTe_2$

3.1.1. Topography

Figure 2 exhibits a topography overview of a cleaved $ZrTe_2$ surface. The hexagonal structure can clearly be recognizedm along with two types of defects: the triangularly shaped elevations with an extension of five protrusions and single missing atoms. Given the crystalline structure of $ZrTe_2$, the top-most layer of this material is expected to consist of Te atoms exclusively. A zoom into an almost defect-free area of $5 \times 5\ \mathrm{nm}^2$, Figure 3a, reveals a distance between the protrusions of approximately 0.38 nm, see the blue line in Figure 3a and corresponding height profile in Figure 3b. Note that this topography resembles those reported in [39], except for the STM-measured distance between the protrusions which is, in our case, in very good agreement with the lattice constant *a*. The presented topographies testify to an excellent overall sample quality and confirm that, primarily, only the top-most Te layer is visualized.

The very few single-site dents observed for positive and negative bias voltage in Figure 2 can certainly be related to missing Te atoms in the Te top-most layer (see also discussion in [40]). In contrast, the more numerous triangularly shaped defects extend over several lattice sites and appear to exhibit different contrast for opposite bias voltages in Figure 2. Very similar defects have been observed on $ZrTe_2$ [41], but also on $TiSe_2$ [40,42,43]. Specifically, the comparison to the latter suggests that these triangular defects may be caused by intercalated Zr atoms, i.e., by Zr at positions between two van der Waals-bound Te layers. The distinctive shape of this type of defect—three neighboring Te atoms in the top-most Te layer appearing bright—for negative V_b (Figure 2 right) compared to the less bright appearance for positive V_b (left) points to an electron-donating defect, in line with its assignment to an intercalated Zr [44]. However, in contrast to the observations of $TiSe_2$ where the intercalated Ti atoms were discussed in relation to a charge density wave (CDW) [42,43], we could not detect any indication of such a CDW in our $ZrTe_2$ (see also STS results below). To the best of our knowledge, a CDW has only been reported for *single-layer* $ZrTe_2$ [45].

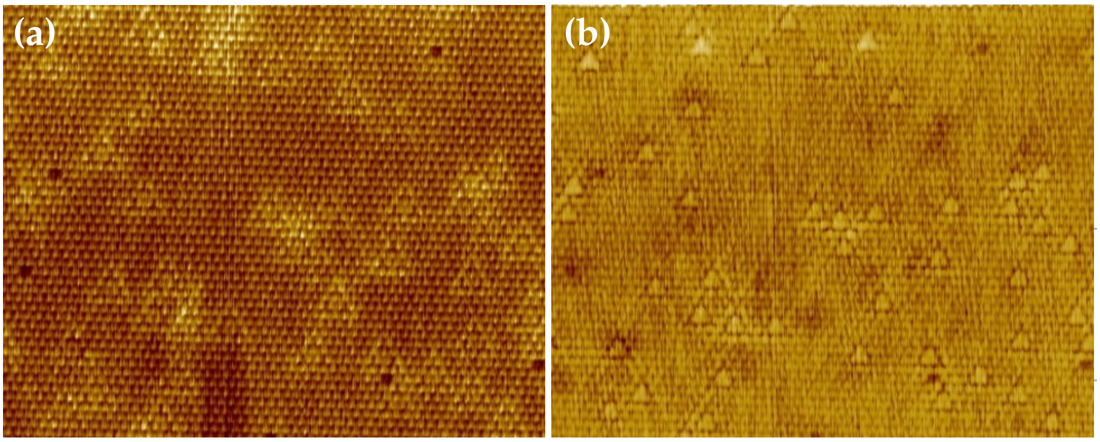

Figure 2. Topography overview of cleaved $ZrTe_2$ over an area of 20×16 nm^2 obtained in dual bias mode, i.e., the two images show exactly the same sample area. (**a**) $V_b = +0.6$ V visualizing empty states and (**b**) $V_b = -0.6$ V, occupied states; $I_{sp} = 200$ pA in both cases. Two different types of defects can be recognized: Single-site vacancies and triangularly shaped defects extending over several lattice sites. The total height range of both topographies is 66 pm.

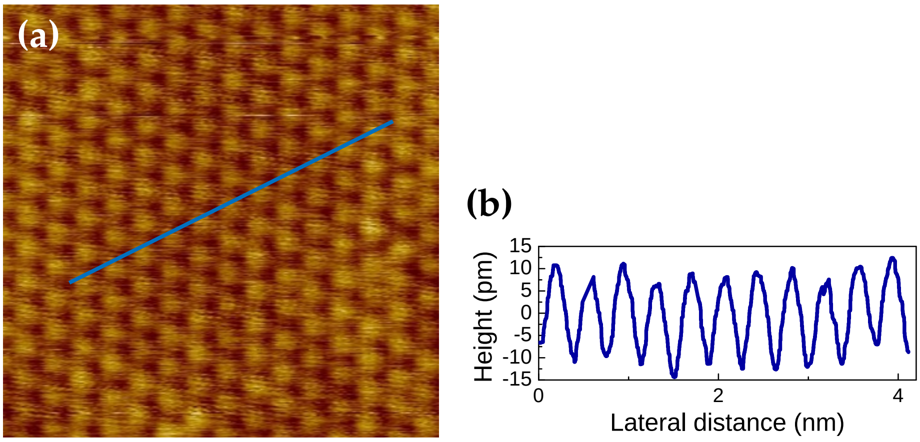

Figure 3. (**a**) Atomically resolved, mostly defect−free area of 5×5 nm^2 on $ZrTe_2$. $V_b = +0.6$ V, $I_{sp} = 200$ pA. (**b**) Height profile obtained along the blue line marked in (a).

3.1.2. Spectroscopy

As mentioned above, much of the recent interest in $ZrTe_2$ stems from its classification as a topological semimetal [28–31]. Hence, STS was conducted on $ZrTe_2$ surfaces. The spectroscopy results presented in Figure 4a were obtained on the surface shown in Figure 4b. The spectrum averaged over the total area does not much differ from the one obtained within the predominantly defect-free area (red rectangle), i.e., we did not observe any significant differences in the local spectra despite the three obvious defects within the total area of Figure 4b. As is clearly revealed in the inset, the density of states (DOS) in close vicinity of the Fermi energy E_F is small but finite (at least at the surface). This behavior is in line with expectations for a semimetal [30] and the dI/dV follows the parabolic shape, as observed for similar semimetals, e.g., $MoTe_2$ [46]. We also note that the formation of a CDW in a single layer of $ZrTe_2$ resulted in a gap of ∼25 meV near E_F [45]. The absence of such a gap in our spectra is then a strong indication for the absence of a CDW in our bulk material, at least down to $T = 4.6$ K.

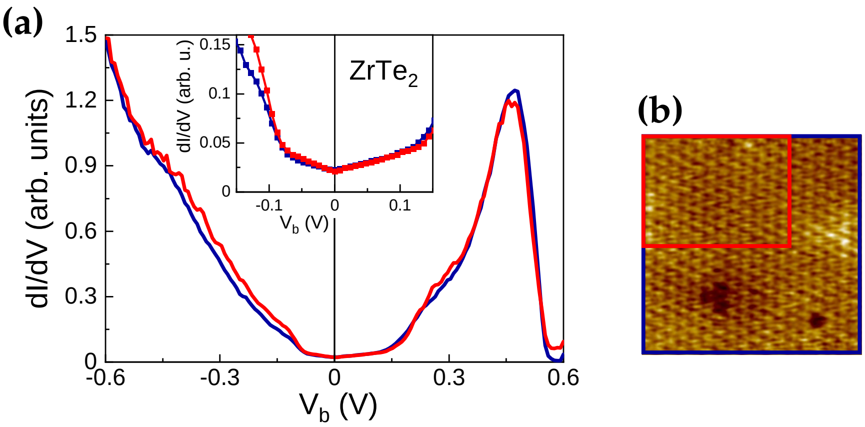

Figure 4. (**a**) Tunneling spectroscopy on a surface of $ZrTe_2$. The inset shows a zoom into the low−energy range of $-0.15\ \text{V} \leq V_b \leq +0.15\ \text{V}$. Spectra were averaged over the total (blue) area and within the red rectangle. (**b**) Topography of total area $6.2 \times 6.2\ \text{nm}^2$ studied to obtain the spectra in (**a**); $V_b = +0.6$ V, $I_{sp} = 200$ pA. The area of the red rectangle ($4.2 \times 3.2\ \text{nm}^2$) is largely free of defects.

It is instructive to compare the measured $\text{d}I/\text{d}V$, Figure 4, to the calculated band structure and DOS of $ZrTe_2$. In Figure 5, the results from [47–49] are reproduced within an energy range $-2\ \text{eV} \leq (E - E_F) \leq +2$ eV. The overall behavior of the total DOS with a very small magnitude at E_F compares favorably to the $\text{d}I/\text{d}V$-data of Figure 4. The peak at positive V_b can be recognized in the calculated DOS, albeit at a somewhat larger energy (0.74 eV in the calculations). Here, we note that in our measurements, the position of this maximum varied slightly between 0.47 V (as in Figure 4) and 0.54 V for different areas on the sample surface. Moreover, a different calculation found a (double-) peak situated at $\sim$0.30 V and $\sim$0.47 V, while the overall parabola-shaped $\text{d}I/\text{d}V$-curve with a minimum close to E_F is not reproduced [50–54]. These comparisons emphasize that details of the local electronic structure of the sample surfaces may vary slightly and may even be different from band structure of the bulk.

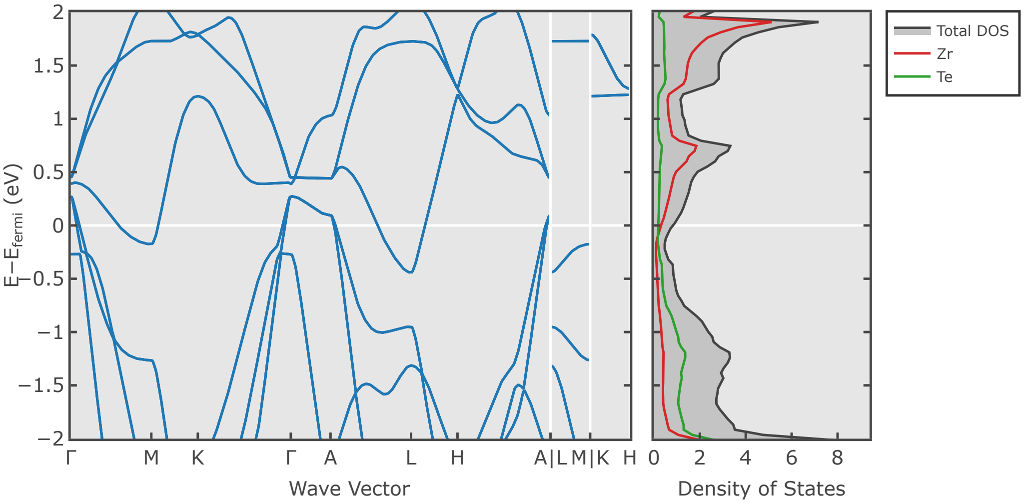

Figure 5. Calculated band structure (**left**) and density of states (**right**) for $ZrTe_2$. Figure reproduced from [49].

The appearance of a weak Kondo effect in $ZrTe_2$ was reported based on transport measurements [32]. Typically, signatures of the Kondo effect can be seen in the $\text{d}I/\text{d}V$ spectra [18,55–57]. Our tunneling spectroscopy, Figure 4, does not provide any indication for a Kondo effect being at play in $ZrTe_2$. It should be noted, however, that the Kondo effect may be suppressed at a sample surface due to a reduced Kondo screening as, e.g., experimentally observed in SmB_6 [58].

3.2. *TmB$_4$*

3.2.1. Topography

Rare-earth tetraborides typically crystallize in the tetragonal ThB$_4$ structure where the B atoms form a continuous 3D network of octahedra and dimers, while the rare-earth atoms lie in planes perpendicular to the c axis forming a two-dimensional (2D) Shastry–Sutherland lattice [37] (cf. Figure 1). The resulting 3D conduction along with the 2D magnetism gives rise to the interest in TmB$_4$ [59]. TmB$_4$ is difficult to cleave, albeit with a slightly higher success rate compared to the hexaborides [25]. Only rarely did we observe the atomically flat surfaces as those shown in Figure 6, where only a few step edges are found (Figure 6b). The height of these step edges is estimated to be 0.41 nm (Figure 6c) and hence, confirms a cleave along the crystallographic c direction.

Zooming into such terraces reveals two different types of termination: Type A is presented in the atomically resolved surface of Figure 7 (left).

Here, the distance between the protrusions is estimated to be about 0.50 nm, corresponding to $a/\sqrt{2} \approx 0.498$ nm. This, along with the linear arrangement of the protrusions, likely indicates a B-terminated surface instead of a Tm one in Figure 1b. Indeed, one may speculate that in the case of the red line, the tip scans over the apex B-atoms of the B octahedra in TmB$_4$, while the blue line scan involves the dimer B atoms (in the latter case, the dimers are alternately aligned parallel and perpendicular to the scan direction). Such an assignment is supported by the distance between the red and blue lines of 0.25 nm $\approx \frac{1}{4}a\sqrt{2}$. A Tm terminated surface is unlikely since an equal number of squares and triangles of Tm would be expected to be observed in that case, along with a distance between Tm atoms of 3.62 Å.

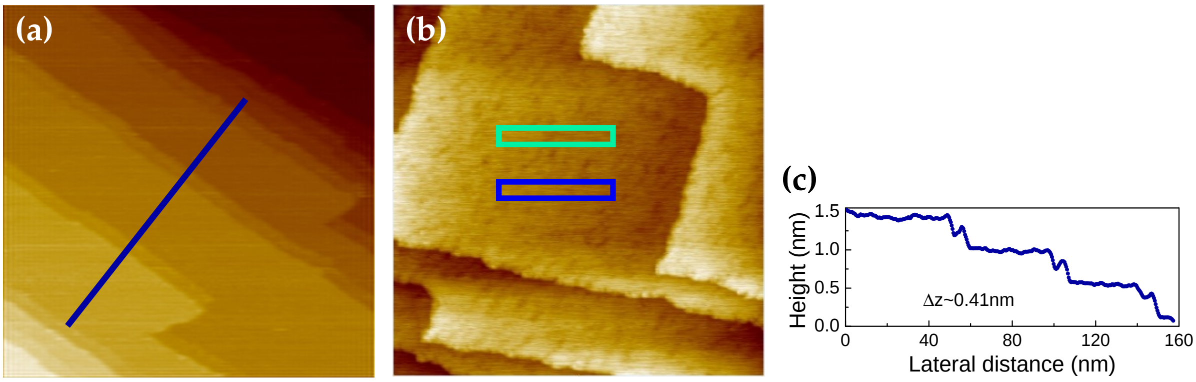

Figure 6. (**a**) Topography overview of cleaved TmB$_4$ over an area of 200 × 200 nm^2 exhibiting several terraces; $V_b = +0.4$ V, $I_{sp} = 600$ pA. (**b**) Zoom into one terrace within the ab plane, area 60 × 60 nm^2, $V_b = +0.8$ V, $I_{sp} = 600$ pA, total height range 770 pm. Numerous individual defects are visible. Green and blue rectangles mark areas within which spectroscopy was conducted, see Figure 9. (**c**) Height scan along the blue line marked in (**a**). The heights of the step edges of about 0.41 nm correspond to the lattice constant $c = 0.398$ nm.

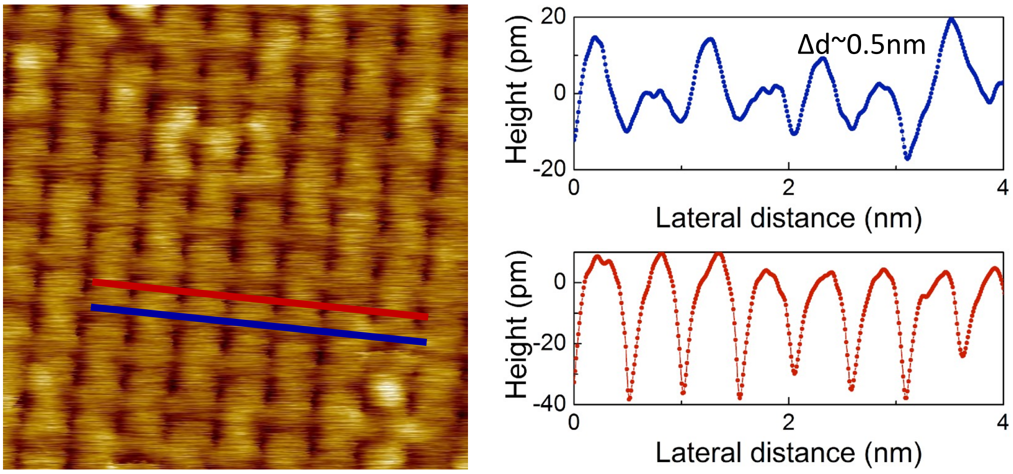

Figure 7. Topography (**left**) on TmB_4 of type A; area of 5 × 5 nm^2, $V_b = +0.15$ V, $I_{sp} = 600$ pA. **Right**: Height scans along the lines of corresponding color marked in the topography. The average distance between protrusions is ∼0.5 nm.

A topography of termination type B is shown in Figure 8. Here, the individual protrusions can more easily be recognized, but there also is a larger number of defects present. The distance between protrusions of ∼0.7 nm fits well to the lattice constant $a = 0.705$ nm. In this case, a Tm termination is unlikely given the overall square arrangement of the protrusions. We note that the topographies of Figures 7 and 8 were obtained within different surface areas of the same sample, i.e., the underlying crystallographic alignment is identical. With the line scans shown in Figure 7 likely taken along the [110] crystallographic direction, the line scans of Figure 8 should correspond to the [100] direction. However, from a merely crystallographic viewpoint, a distance between protrusions of a along the main crystallographic direction is not expected. Here, one possibility that cannot be ruled out is a surface reconstruction. Similarly, superstructures may form at the surface as, e.g., observed on Fe_2O_3 [60]. Another intriguing possibility is an interplay between the electronic and magnetic degrees of freedom. At our measurement temperature of 4.6 K, TmB_4 orders antiferromagnetically with the Tm moments pointing along the [001] direction [33,61] and resulting in a magnetic square unit cell of length a (see, e.g., [33]). One may speculate that this magnetic order has some influence on the topography of Figure 8, either by locally modifying the density of states or, if by chance our W tip had picked up a Tm atom from the surface and turned into a magnetic tip, by directly visualizing the magnetic order (see e.g., [25,62]). These possibilities have to be scrutinized by future investigations.

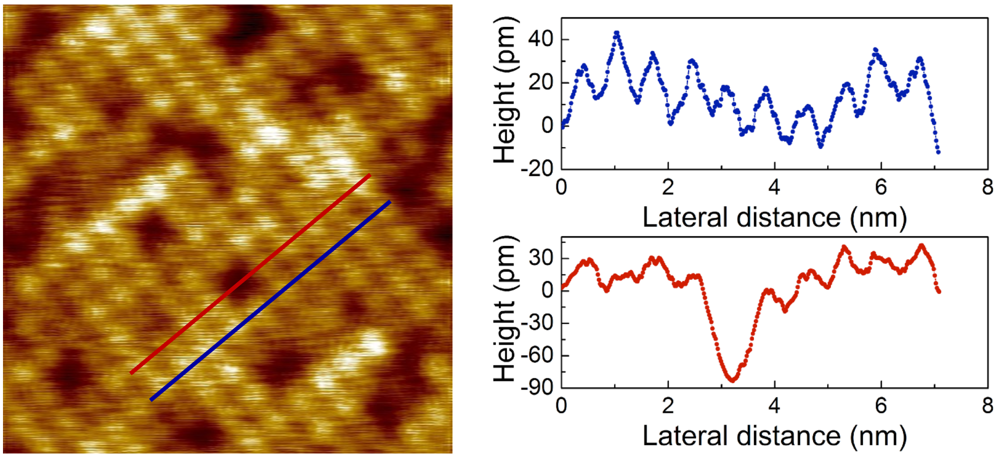

Figure 8. Atomically resolved surface topography type B (**left**) of TmB_4; area of $10 \times 10\ nm^2$, $V_b = +0.4$ V, $I_{sp} = 600$ pA. **Right**: Height scans along the lines of corresponding color marked in the topography. The average distance between protrusions is $\sim$0.7 nm.

3.2.2. Spectroscopy

Tunneling spectroscopy averaged over the areas marked in Figure 6b is presented in Figure 9. In line with TmB_4 being a metal [33,59], there is a large DOS found at E_F. We note that the two dI/dV-curves are qualitatively very similar and rather featureless. The latter is consistent with the small crystal field energy scales suggested in [59] which cannot be resolved by our STS. Moreover, a featureless DOS near E_F has also been predicted in [63] (albeit without magnetic ordering). In contrast, strong peaks in the (spin resolved) DOS close to E_F were reported in [64] based on band structure calculations including strong electronic correlation effects, but not confirmed by our STS data. Here, we should note that the aforementioned calculations are bulk calculations, i.e., they did not take into consideration any surface termination (as, e.g., in the case of slab calculations). As a consequence, the calculated (bulk) DOS and the surface DOS can differ considerably. Clearly, further efforts are required to provide insight into the electronic band structure of TmB_4.

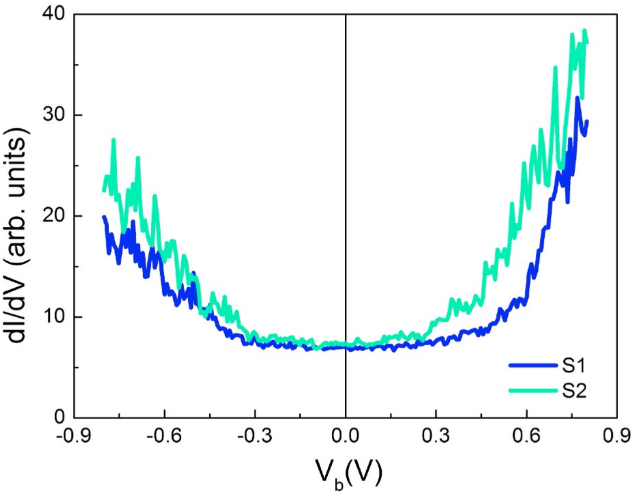

Figure 9. Spectroscopy on TmB_4 within the two areas (denoted as S1 and S2) marked by the same color in Figure 6b. Set point: $V_b = +0.8$ V, $I_{sp} = 0.6$ nA.

4. Discussion

Both materials, $ZrTe_2$ and TmB_4, were successfully prepared for STM/S investigations by in situ cleaving. In the case of $ZrTe_2$, excellent atomically resolved surfaces could be obtained effortlessly, as expected for this 2D compound. The observed defects point to a small number of intercalated Zr (from Figure 2 approximately one intercalated Zr per 56 unit cells) and a tiny amount of Te vacancies (about one vacancy per 500 unit cells) testifying the excellent quality of the material. Nonetheless, these defects may give rise to some amount of doping in this material [65]; in particular, intercalated Zr may act as an electron donor. Such doping effects may contribute to the fact that the calculated electronic band structure of $ZrTe_2$ can only qualitatively be compared to the measured $\mathrm{d}I/\mathrm{d}V$-spectra. In addition, we wish to emphasize again that STS is extremely surface sensitive while the calculations of Refs. [47,48] were conducted for the bulk of the material.

Atomically flat surfaces of TmB_4 could only rarely be located, similar to the case of the hexaborides [25]. Two different types of surfaces could be found, both of which are unlikely to correspond to Tm terminations. Our $\mathrm{d}I/\mathrm{d}V$-data clearly reflect the metallic nature of TmB_4. Beyond this, however, a comparison between the DOS inferred from our STS and the results of band structure calculations is difficult.

Clearly, for both materials further insight from theory as well as from future experiments (including also ARPES) is highly needed. Here, we emphasize that, specifically if non-trivial topology is to be utilized in future applications, the materials properties of the surface play an important role.

Supplementary Materials: The following supporting information can be downloaded at: https://www.mdpi.com/article/10.3390/condmat8010009/s1, Figure S1: EDX of $ZrTe_2$; Table S1: Chemical composition of $ZrTe_2$ obtained by EDX; Figure S2: photograph and Laue pattern of TmB_4 single crystal; Figure S3: XRD of TmB_4. References [37,66] are cited in the Supplementary Materials.

Author Contributions: Conceptualization, S.W.; Resources, V.H., M.S. and N.S.; investigation, M.V.A.C., J.C.S., S.G., K.S. and K.F.; writing—original draft, S.W. and M.V.A.C.; writing—review and editing, S.W., M.V.A.C., M.S. and K.F. All authors have read and agreed to the published version of the manuscript.

Funding: Work at the Max-Planck-Institute for Chemical Physics of Solids in Dresden was funded by the Deutsche Forschungsgemeinschaft (DFG, German Research Foundation), Project No. 449866704. J.C.S. was supported by FAPESP (SP, Brazil) Grants No. 2020/12283-0, No. 2018/11364-7 and No. 2017/10581-1. S.G., K.S. and K.F. were supported by the Slovak Research and Development Agency under contract No. APVV-17-0020, as well as by projects VEGA 2/0032/20, DAAD-57561069, VA SR ITMS2014+ 313011W856 and by the European Microkelvin Platform.

Institutional Review Board Statement: Not applicable.

Data Availability Statement: The data presented in this study are available upon reasonable request from the corresponding author.

Acknowledgments: The authors acknowledge technical help by Hubert Dawczak-Dębicki.

Conflicts of Interest: The authors declare no conflicts of interest.

References

1. Hataugai, Y. Topological aspects of the quantum Hall effect. *J. Phys. Condens. Matter* **1997**, *9*, 2507–25491. [CrossRef]
2. Kane, C.L.; Mele, E.J. Z2 Topological Order and the Quantum Spin Hall Effect. *Phys. Rev. Lett.* **2005**, *95*, 146802. [CrossRef] [PubMed]
3. Bernevig, B.A.; Hughes, T.L.; Zhang, S.C. Quantum spin Hall effect and topological phase transition in HgTe quantum wells. *Science* **2006**, *314*, 1757–1761. [CrossRef] [PubMed]
4. König, M.; Wiedmann, S.; Brüne, C.; Roth, A.; Buhmann, H.; Molenkamp, I.W.; Qi, X.L.; Zhang, S.C. Quantum spin Hall insulator state in HgTe quantum wells. *Science* **2007**, *318*, 766–770. [CrossRef] [PubMed]
5. Fu, L.; Kane, C.L.; Mele, E.J. Topological Insulators in Three Dimensions. *Phys. Rev. Lett.* **2007**, *98*, 106803. [CrossRef] [PubMed]
6. Fu, L.; Kane, C.L. Superconducting proximity effect and Majorana fermions at surface of a topological insulator. *Phys. Rev. Lett.* **2008**, *100*, 096407. [CrossRef]
7. Hasan, H.Z.; Kane, C.L. Colloquium: Topological insulators. *Rev. Mod. Phys.* **2010**, *82*, 3045–3067. [CrossRef]
8. Armitage, N.P.; Mele, E.J.; Vishwanath, A. Weyl and Dirac semimetals in three-dimensional solids. *Rev. Mod. Phys.* **2018**, *90*, 015001. [CrossRef]
9. Wieder, B.J.; Bradlyn, B.; Cano, J.; Nang, Z.; Vergniory, M.G.; Elcoro, L.; Soluyanov, A.A.; Felser, C.; Neu, T.; Regnault, N.; et al. Topological materials discovery from crystal symmetry. *Nat. Rev. Mater.* **2022**, *17*, 196–216. [CrossRef]

10. Lu, D.; Vishik, I.M.; Yi, M.; Moore, R.G.; Shen, Z.X. Angle-resolved photoemission Studies of Quantum Materials. *Annu. Rev. Condens. Matter Phys.* **2012**, *3*, 129–167. [CrossRef]
11. Lv, B.; Qian, T.; Ding, H. Angle-resolved photoemission spectroscopy and its application to topological materials. *Nat. Rev. Phys.* **2019**, *1*, 609–626. [CrossRef]
12. Chen, Y.; Gu, X.; Li, Y.; Du, X.; Yang, L.; Chen, Y. Recent advances in Topological Quantum Materials by angle-resolved Photoemission spectroscopy. *Matter* **2020**, *3*, 1114–1141. [CrossRef]
13. Sobota, J.A.; He, Y.; Shen, Z.X. Topological materials discovery from crystal symmetry. *Rev. Mod. Phys.* **2021**, *93*, 025006. [CrossRef]
14. Rader, O.; Sanchez-Barriga, J.; Rienks, E.D.L.; Varykhalov, A.; Springholz, G.; Yashina, L.V. Angle-resolved photoemission of topological matter: Examples from magnetism, electron correlation, and phase transitions. *Phys. Stat. Sol. B* **2021**, *258*, 2000371. [CrossRef]
15. Hsieh, D.; Xia, Y.; Wray, L.; Qian, D.; Pal, A.; Dil, J.H.; Osterwalder, J.; Meier, F.; Bihlmayer, G.; Kane, C.L.; et al. Observation of unconventional Quantum spin texture in topological insulator. *Science* **2009**, *323*, 919–922. [CrossRef]
16. Xu, N.; Biswas, P.K.; Dil, J.H.; Dhaka, R.S.; Landolt, G.; Muff, S.; Matt, C.E.; Shi, X.; Plumb, N.C.; Radović, M.; et al. Direct observation of the spin texture in SmB_6 as evidence of the topological Kondo insulator. *Nat. Commun.* **2014**, *5*, 4566. [CrossRef]
17. Suga, S.; Sakamoto, K.; Okuda, T.; Miyamoto, K.; Kuroda, K.; Sekiyama, A.; Yamaguchi, J.; Fujiwara, H.; Irizawa, A.; Ito, T.; et al. Spin-Polarized Angle-Resolved Photoelectron Spectroscopy of the So-Predicted Kondo Topological Insulator SmB_6. *J. Phys. Soc. Jpn.* **2014**, *83*, 014705. [CrossRef]
18. Kirchner, S.; Paschen, S.; Chen, Q.; Wirth, S.; Feng, D.; Thompson, J.D.; Si, Q. Colloquium: Heavy-electron quantum criticality and single-particle spectroscopy. *Rev. Mod. Phys.* **2020**, *92*, 011002. [CrossRef]
19. Roushan, P.; Seo, J.; Parker, C.V.; Hor, Y.S.; Hsieh, D.; Qian, D.; Richardella, A.; Hasan, M.Z.; Cava, R.J.; Yazdani, A. Topological surface states protected from backscattering by chiral spin texture. *Nature* **2009**, *460*, 1106–1109. [CrossRef]
20. Zhao, K.; Lv, Y.F.; Ji, S.H.; Ma, X.; Chen, X.; Xue, Q.K. Scanning tunneling microscopy studies of topological insulators. *J. Phys. Condens. Matter* **2014**, *26*, 394003. [CrossRef]
21. Yin, J.X.; Pan, S.H.; Hasan, M.Z. Probing topological quantum matter with Scanning tunnelling microscopy. *Nat. Rev. Phys.* **2021**, *3*, 249–263. [CrossRef]
22. Pirie, H.; Liu, Y.; Soumyanarayanan, A.; Chen, P.; He, Y.; Yee, M.M.; Rosa, P.F.S.; Thompson, J.D.; Kim, D.J.; Fisk, Z.; et al. Imaging emergent heavy Dirac fermions of a topological Kondo insulator. *Nat. Phys.* **2020**, *16*, 52–56. [CrossRef]
23. Allen, J.W. Foreword for special issue of philosophical magazine on: Topological correlated insulators and SmB_6. *Philos. Mag.* **2016**, *96*, 3227–3238. [CrossRef]
24. Alpichshev, Z.; Analytis, J.G.; Chu, J.H.; Fisher, I.R.; Chen, Y.L.; Shen, Z.X.; Fang, A.; Kapitulnik, A. STM Imaging of Electronic Waves on the Surface of Bi_2Te_3: Topologically Protected Surface States and Hexagonal Warping Effects. *Phys. Rev. Lett.* **2010**, *104*, 016401. [CrossRef] [PubMed]
25. Wirth, S.; Schlottmann, P. An STM perspective on hexaborides: Surface states of the Kondo insulator SmB_6. *Adv. Quantum Technol.* **2021**, *92*, 011002. [CrossRef]
26. Zhang, H.; Pincelli, T.; Jozwiak, C.; Kondo, T.; Ernstorfer, R.; Sato, T.; Zhou, S. Angle-resolved photoemission spectroscopy. *Nat. Rev. Methods Prim.* **2022**, *2*, 54. [CrossRef]
27. Manzeli, S.; Ovchinnikov, D.; Pasquier, D.; Kis, O.V.Y.A. 2D transition metal dichalcogenides. *Nat. Rev. Mater.* **2017**, *2*, 17033. [CrossRef]
28. Tsipas, P.; Tsoutsou, D.; Fragkos, S.; Sant, R.; Alvarez, C.; Okuno, H.; Renaud, G.; Alcotte, R.; Baron, T.; Dimoulas, A. Massless Dirac Fermions in $ZrTe_2$ Semimetal Grown on InAs(111) by van der Waals Epitaxy. *ACS Nano* **2018**, *12*, 1696–1703. [CrossRef]
29. Tian, Y.; Ghassemi, N.; Ross, Jr., J.H. Topological nodal line in $ZrTe_2$ demonstrated by nuclear magnetic resonance. *Phys. Rev. B* **2020**, *102*, 165149. [CrossRef]
30. Kar, I.; Chatterjee, J.; Harnagea, L.; Kushnirenko, Y.; Fedorov, A.V.; Shrivastava, D.; Büchner, B.; Mahadevan, P.; Thirupathaiah, S. Metal-chalcogen bond-length induced electronic phase transition from semiconductor to topological semimetal in ZrX_2 (X = Se and Te). *Phys. Rev. B* **2020**, *101*, 165122. [CrossRef]
31. Nguyen, T.; Aryal, N.; Pokharel, B.K.; Harnagea, L.; Mierstchin, D.; Popović, D.; Graf, D.E.; Shrestha, K. Fermiology of the Dirac type-II semimetal candidates (Ni,Zr)Te_2 using de Haas–van Alphen oscillations. *Phys. Rev. B* **2022**, *106*, 075154. [CrossRef]
32. Wang, Y.; Xie, C.; Li, J.; Du, Z.; Cao, L.; Han, Y.; Zu, L.; Zhang, H.; Zhu, H.; Zhang, X.; et al. Weak Kondo effect in the monocrystalline transition metal dichalcogenide $ZrTe_2$. *Phys. Rev. B* **2021**, *103*, 174418. [CrossRef]
33. Siemensmeyer, K.; Wulf, E.; Mikeska, H.J.; Flachbart, K.; Gabáni, S.; Mat'aš, S.; Priputen, P.; Efdokimova, A.; Shitsevalova, N. Fractional Magnetization Plateaus and Magnetic Order in the Shastry-Sutherland Magnet TmB_4. *Phys. Rev. Lett.* **2008**, *101*, 177201. [CrossRef]
34. Bhowmick, D.; Sengupta, P. Topological magnon bands in the flux state of Shastry-Sutherland lattice model. *Phys. Rev. B* **2020**, *101*, 214403. [CrossRef]
35. Orendáč, M.; Gabáni, S.; Farkašovský, P.; Gažo, E.; Kačmarčík, J.; Marcin, M.; Pristáš, G.; Siemensmeyer, K.; Shitsevalova, N.; Flachbart, K. Ground state and stability of the fractional plateau phase in metallic Shastry-Sutherland system TmB_4. *Sci. Rep.* **2021**, *11*, 6835. [CrossRef]

36. Choi, H.; Zhu, W.; Cary, S.K.; Winter, L.E.; Huang, Z.; McDonald, R.D.; Mocko, V.; B. L. Scott, P.H.T.; Thompson, J.D.; Kozimor, S.A.; et al. Experimental and theoretical study of topology and electronic correlations in PuB_4. *Phys. Rev. B* **2018**, *97*, 201114(R). [CrossRef]
37. Shitsevalova, N. Crystal chemistry and crystal growth of Rare-earth borides. In *Rare-Earth Borides*; Inosov, D., Ed.; Jenny Stanford Publishing: Singapore, 2021; pp. 1–243. [CrossRef]
38. Omicron Nanotechnology GmbH. Taunusstein (Germany).
39. Muhammad, Z.; Zhang, B.; Lv, H.; Shan, H.; Rehman, Z.; Chen, S.; Sun, Z.; Wu, X.; Zhao, A.; Song, L. Transition from Semimetal to Semiconductor in $ZrTe_2$ Induced by Se Substitution. *ACS Nano* **2020**, *14*, 835–841. [CrossRef]
40. Hildebrand, B.; Didiot, C.; Novello, A.; Monney, G.; Scarfato, A.; Ubaldini, A.; Berger, H.; Bowler, D.; Renner, C.; Aebi, P. Doping Nature of Native Defects in $1T$-$TiSe_2$. *Phys. Rev. Lett.* **2014**, *112*, 197001. [CrossRef]
41. Ren, M.Q.; Han, S.; Fan, J.Q.; Wang, L.; Wang, P.; Ren, W.; Peng, K.; Li, S.; Wang, S.Z.; Zheng, F.W.; et al. Semiconductor–Metal Phase Transition and Emergent Charge Density Waves in $1T$-ZrX_2 (X = Se and Te) at the Two-Dimensional Limit. *Nano Lett.* **2022**, *22*, 476–484. [CrossRef]
42. Novello, A.; Hildebrand, B.; Scarfato, A.; Didiot, C.; Monney, G.; Ubaldini, A.; Berger, H.; Bowler, D.R.; Aebi, P.; Renner, C. Scanning tunneling microscopy of the charge density wave in $1T$-$TiSe_2$ in the presence of single atom defects. *Phys. Rev. B* **2015**, *92*, 081101. [CrossRef]
43. Hildebrand, B.; Jaouen, T.; Didiot, C.; Razzoli, E.; Monney, G.; Mottas, M.L.; Ubaldini, A.; Berger, H.; Barreteau, C.; Beck, H.; et al. Short-range phase coherence and origin of the $1T$-$TiSe_2$ charge density wave. *Phys. Rev. B* **2016**, *93*, 125140. [CrossRef]
44. Wan, J.; Lacey, S.D.; Dai, J.; Bao, W.; Fuhrer, M.S.; Hu, L. Tuning two-dimensional nanomaterials by intercalation: Materials, properties and applications. *Chem. Soc. Rev* **2016**, *45*, 6742–6765. [CrossRef] [PubMed]
45. Yang, L.N.; Xu, Y.J.; Li, Q.Y.; Meng, Y.X.; Zhao, Y.F.; Li, S.C. Coexistence of the charge density wave state and linearly dispersed energy band in $1T$-$TiSe_2$ monolayer. *Appl. Phys. Lett.* **2022**, *120*, 073105. [CrossRef]
46. Iaia, D.; Chang, G.; Chang, T.R.; Hu, J.; Mao, Z.; Lin, H.; Yan, S.; Madhavan, V. Searching for topological Fermi arcs via quasiparticle interference on a type-II Weyl semimetal $MoTe_2$. *NPJ Quantum Mater.* **2018**, *3*, 38. [CrossRef]
47. Jain, A.; Ong, S.P.; Hautier, G.; Chen, W.; Richards, W.D.; Dacek, S.; Cholia, S.; Gunter, D.; Skinner, D.; Ceder, G.; et al. Commentary: The Materials Project: A materials genome approach to accelerating materials innovation. *APL Mater.* **2013**, *1*, 011002. [CrossRef]
48. Munro, J.M.; Latimer, K.; Horton, M.K.; Dwaraknath, S.; Persson, K.A. An improved symmetry-based approach to reciprocal space path selection in band structure calculations. *NPJ Comput. Mater.* **2020**, *6*, 112. [CrossRef]
49. Data Retrieved from the Materials Project for $ZrTe_2$ (mp-1018107) from Database Version v2021.11.10. Available online: https://materialsproject.org/materials/mp-1018107 (accessed on 2 December 2022).
50. Available online: https://topologicalquantumchemistry.org/#/detail/653213 (accessed on 2 December 2022).
51. Bradlyn, B.; Elcoro, L.; Cano, J.; Vergniory, M.G.; Wang, Z.; Felser, C.; Aroyo, M.I.; Bernevig, B.A. Topological quantum chemistry. *Nature* **2017**, *547*, 298–305. [CrossRef]
52. Vergniory, M.G.; Elcoro, L.; Felser, C.; Regnault, N.; Bernevig, B.A.; Wang, Z. A complete catalogue of high-quality topological materials. *Nature* **2019**, *566*, 480–485. [CrossRef]
53. Vergniory, M.G.; Wieder, B.J.; Elcoro, L.; Parkin, S.S.P.; Felser, C.; Bernevig, B.A.; Regnault, N. All topological bands of all nonmagnetic stoichiometric materials. *Science* **2022**, *376*, eabg9094. [CrossRef]
54. Available online: https://www.cryst.ehu.es (accessed on 2 December 2022).
55. Li, J.T.; Schneider, W.D.; Berndt, R.; Delley, B. Kondo scattering observed at a single magnetic impurity. *Phys. Rev. Lett.* **1998**, *80*, 2893–2896. [CrossRef]
56. Madhavan, V.; Chen, W.; Jamneala, T.; Crommie, M.F.; Wingreen, N.S. Tunneling into a single magnetic atom: Spectroscopic evidence of Kondo resonance. *Science* **1998**, *280*, 567–569. [CrossRef]
57. Wirth, S.; Steglich, F. Exploring heavy fermions from macroscopic to microscopic length scales. *Nat. Rev. Mater.* **2016**, *1*, 16051. [CrossRef]
58. Jiao, L.; Rößler, S.; Kim, D.J.; Tjeng, L.H.; Fisk, Z.; Steglich, F.; Wirth, S. Additional energy scale in SmB_6 at low temperature. *Nat. Commun.* **2016**, *7*, 13762. [CrossRef]
59. Shin, J.; Schlesinger, Z.; Shastry, B.S. Kondo-Ising and tight-binding models for TmB_4. *Phys. Rev. B* **2017**, *95*, 205140. [CrossRef]
60. Ossowski, T.; Pabisiak, T.; Kiejna, A.; Palotás, K.; Bauer, E. Simulation of STM Images of Hematite α-Fe_2O_3 Surfaces: Dependence on distance and bias. *J. Phys. Chem. C* **2021**, *125*, 26711–26717. [CrossRef]
61. Michimura, S.; Shigekawa, A.; Iga, F.; Takabatake, T.; Ohoyama, K. Complex Magnetic Structures of a Shastry–Sutherland Lattice TmB_4 Studied by Powder Neutron Diffraction Analysis. *J. Phys. Soc. Jpn.* **2009**, *78*, 024707. [CrossRef]
62. Enayat, M.; Sun, Z.; Singh, U.R.; Aluru, R.; Schmaus, S.; Yaresko, A.; Liu, Y.; Lin, C.; Tsurkan, V.; Loidl, A.; et al. Real-space imaging of the atomic-scale magnetic structure of $Fe_{1+y}Te$. *Science* **2014**, *345*, 653–656. [CrossRef]
63. Data Retrieved from the Materials Project for TmB_4 (mp-568143) from Database Version v2021.11.10. Available online: https://materialsproject.org/materials/mp-568143 (accessed on 5 December 2022).
64. Pakhira, N.; Krishna, J.; Nandy, S.; Maitra, T.; Taraphder, A. Electronic structure of metallic tetra-boride TmB_4: An LDA+DMFT study. *arXiv* **2018**, arXiv:1807.05388.

65. Liu, J.; Li, B.; Li, Q. Two-dimensional doped materials. *Magnetochemistry* **2022**, *8*, 172. [CrossRef]
66. Tanaka, T.; Nishitani, R.; Oshima, C.; Bannai, E.; Kawai, S. The preparation and properties of CeB_6, SmB_6, and GdB_6. *J. Appl. Phys.* **1980**, *45*, 3877–3883. [CrossRef]